RSC Advances

ROYAL SOCIETY OF CHEMISTRY

PAPER

View Article Online
View Journal | View Issue

Check for updates

Cite this: *RSC Adv.*, 2021, **11**, 29453

Reduction and oxidation kinetics of $NiWO_4$ as an oxygen carrier for hydrogen storage by a chemical looping process†

P. E. González-Vargas, J. M. Salinas-Gutiérrez, M. J. Meléndez-Zaragoza, J. C. Pantoja-Espinoza, A. López-Ortiz* and V. Collins-Martínez

$NiWO_4$ with a volumetric storage density (VSD) of 496 g L^{-1} was studied to evaluate its H_2 storage potential as an oxygen carrier under a chemical looping (CL) process scheme. The material was synthesized by precipitation and calcined at 950 °C for 5 hours in air. Characterization consisted in XRD, BET surface area, SEM and EDS analysis. $NiWO_4$ hydrogen storage reduction-oxidation evaluation was performed by TGA using 5% v H_2/Ar and 2.2% v H_2O/Ar at 800 °C. Global kinetics for the reduction step was studied from 730 to 870 °C using 2 to 5% v of H_2/Ar. While oxidation kinetics was examined from 730 to 870 °C using 0.8 to 2.2% v H_2O/Ar. A hydrogen storage multicycle stability test was performed by exposing $NiWO_4$ to 17 consecutive redox cycles. XRD results of the synthesized material indicate $NiWO_4$ as the only crystalline phase. Fully reduced material found only W and Ni species, while reoxidation led back to $NiWO_4$. BET surface area of synthesized material was 4.25 m^2 g^{-1}. SEM results showed fresh $NiWO_4$ composed of non-porous large particles (1–5 μm). After reduction, the material shown a porous coral-like morphology with particles between 50 to 100 nm. EDS analysis results confirmed the compositions of the reduced (Ni + W) and fully oxidized $NiWO_4$ species, respectively. Oxygen carrier reaction conversions for both reduction and regeneration steps were 100%. Global kinetic studies indicate a first order reaction for the two reduction steps and during oxidation, with activation energies of 22.1, 48.4 and 53.4 kJ mol^{-1} for the two reduction and oxidation steps, respectively. $NiWO_4$ multicycle stability test shown no loss of VSD and fast reduction and oxidation kinetics under the studied conditions after seventeen consecutive redox cycles, which confirms the potential of this material with respect to current oxygen carriers reported in the literature for hydrogen storage applications.

Received 1st July 2021
Accepted 25th August 2021

DOI: 10.1039/d1ra05077j

rsc.li/rsc-advances

Introduction

Energy today is strongly related to the economic growth of countries around the world and plays an important role in the improvement of living standards, healthcare and educational services, digital information connections and in general an increased productivity.

Although it is difficult to predict the world's energy consumption in a precise way in the future, it is a fact that this will significantly increase in the coming decades due to the constant growth of the human population and economies worldwide, which in turn demands the consumption of diverse natural resources to satisfy human basic needs.

Such is the case of fossil fuels, mainly used to obtain electricity, transport and artificial air conditioning of buildings. It is due to the decrease in reserves of these fuels and the environmental impacts that these generate that the scientific community around the world are searching for alternative energy sources and sustainable raw materials.[1]

In recent times, hydrogen (H_2) has been of great interest, since it is considered as raw material for a wide variety of processes. For example, with nitrogen in the synthesis of ammonia, with CO and CO_2 to produce methanol, in the manufacture of pharmaceuticals, production of hydrogen peroxide, in the electronics and petrochemical industries and to produce numerous chemical products in various processes.[1–3] Moreover, hydrogen can be considered as a clean energy carrier, like electricity, which can be produced from various local resources such as renewable and nuclear energy. In the long-term, hydrogen is expected to reduce the dependence on fossil fuels and consequently the emission of greenhouse gases and other pollutants. Currently, hydrogen production accounts for around 2% of the primary energy demand.[4] One of the main disadvantages of the use of hydrogen as an energy carrier deals with its relatively low volumetric energy density (8 MJ L^{-1}), even though this presents a high gravimetric energy density (120 MJ

Departamento de Ingeniería y Química de Materiales, Centro de Investigación en Materiales Avanzados, S.C., Miguel de Cervantes 120, Chihuahua, Chih., 31109, México. E-mail: alejandro.lopez@cimav.edu.mx; Tel: +52 6144394815

† Electronic supplementary information (ESI) available. See DOI: 10.1039/d1ra05077j

kg^{-1}).[5] This low value in volumetric energy density makes very difficult to efficiently transport hydrogen because it needs to be either compressed or liquified, consequently employing large amounts of energy in the process. Therefore, it is necessary to develop better technologies, such as transportation and storage, to make it a more feasible energy vector.[6]

The volumetric storage density (VSD) is a common way to measure the storage capacity of hydrogen in this field and it consists in the weight of hydrogen stored per unit volume of the storage media (g L^{-1}). Typically, the VSD for the liquid hydrogen is 70 g L^{-1}. However, a considerable amount of energy must be consumed to maintain the high pressure and low hydrogen liquefaction temperature.[7]

Nowadays, various physical and chemical methods for hydrogen storage have been proposed. Such as high-pressure and cryogenic-liquid storage, adsorptive storage on high-surface-area adsorbents, chemical storage in metal hydrides and complex hydrides, storage in boranes, carbon materials, and metal organic frameworks.[8,9] However, each storage method has its advantages and difficulties due to safety, size, weight, cost and efficiency requirements.[10]

An innovative alternative to the actual hydrogen storage technologies has been proposed in recent years, which deals with the chemical looping process (CL). This CL offers many advantages over current technologies such as high efficiency, economic and ecological materials, and proven technical feasibility.[11] This technique employs oxygen carrier materials with very high VSD values (≈ 200 g L^{-1}) that are exposed to a redox cycle. This CL process for hydrogen storage use carrier materials that once reduced by hydrogen convert to metals. These metals are then, in an oxidation step, reacted with steam to release hydrogen as a product of this reaction.

There are a large number of materials that have been evaluated under the CL concept for many thermochemical applications. However, there are a unique number of features that are required for an oxygen carrier to be successfully applied in the area of CL and specifically to CL hydrogen storage. First, the material must retain activity after a fair number of redox cycles, while avoiding deactivation by sintering (thermal stability), possess a high VSD and hydrogen storage capacity, avoid the use of toxic and harmful (to the environment) materials in its composition, to be constituted of abundant and non-expensive materials and finally, to present reasonable reduction and oxidation kinetics.

The use of redox reactions with metal oxides (MeO) under a CL reaction scheme for hydrogen storage is based on reactions (1) and (2).[8]

$$Me_xO_y + yH_2 \rightarrow xMe + yH_2O \tag{1}$$

$$xMe + yH_2O \rightarrow Me_xO_y + yH_2 \tag{2}$$

In order to be used in a CL process, MeO species must be thermally stable to withstand temperature gradients which are subjected during the process, to be able to store and release lattice oxygen at reaction conditions, and have good availability and affordable costs.[12] The most common MeO reported is iron oxide in its different oxidation states (Fe_3O_4 and Fe_2O_3) and this process is commonly known as the steam-iron process. This process consists in the reduction of iron oxide with H_2 for storage purposes, and the subsequent release of H_2 when oxidizing Fe with steam.[13–15] The theoretical maximum storage capacity of H_2 in this process is 4.8% w of Fe,[8] *i.e.*, based on the Fe as the only solid reactant. It is also reported a VSD of 374 g L^{-1} for iron oxides, which is considered a high value.[5] However, most of the oxygen carriers proposed in various research studies employ the impregnation and/or support on different materials of iron oxide to improve the thermal stability and to avoid the material sintering.[13,15–18] This causes the generation of an additional inert load to the reactors, which in turn leads to the reduction of up to 3 times the storage capacity of H_2 based on the total solids in the reactive species (including Fe).

In other studies, related to the CL, it has been reported that some mixed metal oxides used as oxygen carriers, such as perovskites and ilmenites (ABO_3), are resistant to high temperatures.[19,20] These investigations attribute the thermal resistance of the material to the cation A, while high valence B cations would contribute to the catalytic action. An example of these materials is ilmenite ($FeTiO_3$) that is reported by Schwebel *et al.*[21] as an oxygen carrier for H_2 and CO as reducing gases. These materials were reported without the addition of extra inert species (supports) for their operation, a feature that can be of advantage towards the CL storage of H_2.

One strategy to improve the sintering resistance of the material has been to include refractory materials in combination with iron oxides such as Al_2O_3, $MgAlO_4$ and SiO_2.[22–24] However, the introduction of an inert material has an important impact on the reduction of the VSD of the resulting oxygen carrier. In addition, many studies have focused in the increase of the oxygen-carrier reduction kinetics with hydrogen such as Otsuka *et al.*[25] that added Rh and/or Ir to Fe/Fe_3O_4 resulting in a small VSD of 68 g L^{-1} of this material. Furthermore, Takenaka *et al.*[26] employed a co-doped $Cu–Cr–FeO_x$ sample showing a VSD of 65 g L^{-1} at 980 K. In these studies, the addition of Rh, Ir, Pd, Cr can significantly improve the activity and kinetics of iron oxides. However, these not only added high-cost materials to the oxygen carriers, but also presented reduced VSD values compared to plain iron oxide (374 g L^{-1}),[5] thus restraining their commercial utilization and causing researches to focus their investigations on earth-abundant materials. That is the case of oxygen carriers such as $Co_{0.25}Fe_{2.75}O_4$, $Zn_{0.25}Fe_{2.75}O_4$, $Cu_{0.25}Fe_{2.75}O_4$, $Mn_{0.25}Fe_{2.75}O_4$ and $Ni_{0.25}Fe_{2.75}O_4$ for CL hydrogen storage as reported by Xiao *et al.*[5] Their results showed that $Co_{0.25}Fe_{2.75}O_4$ exhibited an acceptable VSD of 62.47 g L^{-1} and average hydrogen production rate of 132 μmol g^{-1} min^{-1} with a fair performance after 10 redox cycles at 550 °C.

Recently, it has been reported that the oxygen diffusion process is one of the main rate-limiting steps towards the oxidation–reduction reactions within the oxygen carrier material under a CL reaction scheme. Li *et al.*,[27] studied the partial oxidation of methane employing a transient pulse injection experimental reactor. They found that the rate-limiting step was the bulk oxygen diffusion determined by the surface O coverage over the oxygen carrier, while the methane activation mechanism did not significantly affect the reaction kinetics towards the syngas production. In another other study, Fleischer *et al.*,[28] found that the high ethylene selectivity consists in limiting the fast oxygen diffusion and thereby suppressing the surface over-oxidation. In tuning the oxygen diffusion process within Fe-oxide oxygen carriers several studies have employed different metals such as Ni,[29,30] Ce,[31,32] Cu,[33,34] Co[35] and Mn.[36] Xiao *et al.*,[37] investigated the effects of spatial structure of oxygen carrier materials on the CL process to tune the oxygen diffusion and the product selectivity under the methane partial oxidation process using a series of Ni–Fe–Zr model oxygen carriers with different spatial structure. Furthermore, mixed ion-electron materials (MIEM) with excellent ion and electron conductivity have been intensively used in fuel cells. Some of those materials have been employed as supports to improve the sintering resistance of iron oxides and at the same time improve their oxygen-ion conductivity to enhance reactivity. Recently Cho *et al.*,[38] employed 60% w $Gd_{0.1}Ce_{0.9}O_{2-\delta}$ to support Fe_2O_3 in methane partial oxidation at 900 °C and achieved a high redox stability over repetitive redox cycles. While, Xiao *et al.*,[39] employed $Gd_xCe_{2-x}O_{2-\delta}$ as MIEM support for Fe_2O_3 oxygen carrier in the Reverse Water Gas Shift Chemical Looping (RWGS-CL). They found a remarkable linear relationship between the oxygen-ion conductivity and the CO_2 reactivity. Therefore, the oxygen diffusion process as well as the oxygen-ion conductivity within the oxygen carrier will inevitably affect the hydrogen storage performance of the material.

Moreover, tungstate materials such as $CoWO_4$ and $NiWO_4$ have been reported to present relatively high ion conductivities. $CoWO_4$ exhibits an ion conductivity in the range 10^{-8} to 10^{-3} $ohm^{-1}\ cm^{-1}$ in a temperature range of 200–500 °C,[40] while $NiWO_4$ presents values in the range of 10^{-6} to 10^{-4} $ohm^{-1}\ cm^{-1}$ for the same temperature range.[41] These tungstate ion conductivities are due to their monoclinic structure,[41] in which the oxygen ions are hexagonally close packed and the metal ions occupy only a quarter of all the octahedral interstices. Furthermore, high temperature conductivity measurements have been reported for several single crystal $M^{2+}WO_4$ (M^{2+} = Mn, Co, Ni, Cu) transition metal tungstates.[39,42] Therefore, in principle metal tungstates such as $CoWO_4$ and $NiWO_4$ can be expected to present high oxygen diffusions as materials to be used under a hydrogen storage CL reaction scheme.

Additionally, cobalt tungstate ($CoWO_4$) was proposed by De Los Ríos *et al.*,[12,43,44] doped with nickel (Ni) as a catalyst, and reported to be highly stable after 10 redox cycles. This type of material presented high thermal stability under cyclic redox conditions due to a solid diffusional reactive barrier[45] and required lower operating temperatures compared to other mixed metal oxides.

Hydrogen reduction of another tungstate material, nickel tungstate ($NiWO_4$), has been recently reported by Ahmed *et al.*[46] to obtain Ni–W and WC alloys for the manufacturing of microstructured tools. From a theoretical point of view, this material can be considered as a good candidate for CL hydrogen storage purposes. The global CL hydrogen storage redox reactions for $NiWO_4$ are the following:

$$NiWO_4 + 4H_2 \rightarrow Ni + W + 4H_2O \quad (3)$$

$$Ni + W + 4H_2O \rightarrow NiWO_4 + 4H_2 \quad (4)$$

While reaction (3) was reported by Ahmed *et al.*,[46] reaction (4) is proposed in the present research. According to recent studies by Lopez-Ortiz *et al.*,[47] who performed a thermodynamic analysis on $NiWO_4$, it was determined this material is able to react in a methane-steam redox cycle at a temperature range of 700–1000 °C. Furthermore, it is quite remarkable that the theoretical VSD of this material is 496 g L^{-1}. This large number can be explained from the fact that mixed metal oxides provide a greater amount of hydrogen storage. This is due to the fact that both metals in $NiWO_4$ crystalline structure are susceptible to be reduced under a hydrogen atmosphere (reaction (3)) to their metallic states (Ni + W) and be oxidized back to the original $NiWO_4$ structure under steam atmospheres to release hydrogen (reaction (4)). Therefore, no inert material is added to this oxygen carrier and all its mass can be used for hydrogen storage purposes.

Moreover, $NiWO_4$ meets all the necessary characteristics of a suitable material for a CL hydrogen storage application, as it is formed from relatively abundant compounds, that presumably present similar high thermal stability of other tungstate oxides, and possesses a high theoretical VSD. Therefore, $NiWO_4$ was selected in this research to be synthesized, characterized (through XRD, SEM and BET), evaluated on its hydrogen storage capacity by thermogravimetric analysis (TGA), studied to establish its reduction and oxidation global kinetics and thermal stability by a multicycle redox test. All of these to determine its feasibility as a hydrogen storage oxygen carrier under a CL reaction scheme.

Methodology

Synthesis

The $NiWO_4$ was synthesized by the chemical precipitation method using solutions at room temperature under constant stirring, as reported by Song *et al.*[48] Briefly, 100 mL of 0.7 M precursors salts $Na_2WO_4 \cdot 2H_2O$ (Sigma Aldrich sodium tungstate dihydrate, white crystals, 99.9% w pure, melting point at 698 °C, and relative density of 4.18 g cm^{-1}) and $Ni(NO_3)_2 \cdot 6H_2O$ (Sigma Aldrich nickel(II) nitrate hexahydrate, emerald green crystals, 99.9% w pure, melting point at 56.7 °C, and relative density of 2.05 g cm^{-1}) solutions under strongly magnetic stirring at room temperature were mixed together drop by drop using a peristaltic pump. Once the precipitate was obtained, it was filtered and washed repeatedly with deionized water and then dried at 100 °C for 2 hours. The resulting solid was pulverized in an agate mortar. This powder was then calcined at 950 °C for 5 hours in a ceramic crucible and allowed to cool at room temperature in a desiccator. The powder was vialed for further characterization and tests.

Thermodynamic analysis

$NiWO_4$ reduction with hydrogen has been previously reported and its thermodynamics.[46,49,50] However, regeneration conditions using H_2O have not been attempted. Therefore, a thermodynamic sensitivity analysis using a Gibbs reactor in Aspen Plus software was carried out. This Gibbs reactor employs the Gibbs free energy minimization technique to obtain the equilibrium compositions for each gaseous and solid species within each reaction system. This technique is fully described elsewhere.[51] The thermodynamic reaction system composed by the following gaseous species: $H_{2(g)}$ and $H_2O_{(g)}$. The solid species included in the system were $NiWO_4$, NiO, WO_2, WO_3, Ni and W. The feed stream to the reactor was fixed to 1 kmol h^{-1} of each Ni and W, while the amount of steam feed was varied from 3 to 14 kmol h^{-1}. In addition, the reactor temperature was varied from 600 to 950 °C. This thermodynamic analysis will provide experimental conditions where fully regeneration of $NiWO_4$ can be expected.

Hydrogen storage performance evaluation

The redox behavior of the $NiWO_4$ powder was followed by a TA-Instruments TGA model Q500, following the weight change (% w) signal with respect to time. All redox experiments were carried out at atmospheric pressure, the total gas flowrate through the sample was 100 mL min^{-1} and the amount of $NiWO_4$ was of *ca.* 20 mg placed in a platinum-made sample holder.

A first redox cycle experiment was performed at a constant temperature of 800 °C using 5% v H_2/Ar and 2.2% v H_2O/Ar for reduction and reoxidation, respectively, aiming to evaluate the initial $NiWO_4$ hydrogen storage by comparing the degree of reduction and oxidation in a complete redox cycle. This test then was compared with results of other oxygen carriers previously reported in the literature.

Characterization

Characterization of the calcined sample was examined to study its crystalline structure on a Panalytical X'Pert PRO powder diffractometer using Cu-Kα radiation generated at 40 kV and 30 mA. BET specific surface area was examined by N_2 adsorption–desorption isotherms with a NOVA 4200e surface area and pore size analyzer apparatus, morphology and microanalysis composition by scanning electron microscopy (SEM), and energy dispersive X-ray spectroscopy (EDS) were examined on a JEOL JSM-7401F field emission scanning electron microscope.

The XRD, SEM and EDS analyses were performed on the fresh synthesized sample, after the first thermogravimetric analysis (TGA) reduction (R), after one TGA redox cycle (RO), after a second TGA reduction (ROR) and after 17 TGA redox cycles. This was, in order to characterize the material during its exposure to different steps of reduction and oxidation cycles, as well as to evaluate the stability of $NiWO_4$ to determine the chemical species present in each stage and establish their reaction paths.

Global kinetic study

In order to evaluate the reduction and oxidation kinetics, different temperatures and gas concentrations were used. Table 1 shows 18 experimental conditions that were employed for the global kinetic study.

Table 1 Experimental conditions for the global kinetic study

	Temperature								
Reactant atmosphere	730 °C			800 °C			870 °C		
H_2/Ar (% v)	2.0	3.4	5.0	2.0	3.4	5.0	2.0	3.4	5.0
H_2O/Ar (% v)	0.8	1.5	2.2	0.8	1.5	2.2	0.8	1.5	2.2

Prior to each TGA test, the sample was heated in an inert atmosphere (Ar) to reach the targeted experimental temperature (730, 800 or 870 °C) and then followed by an isothermal step under a reducing (H_2/Ar) or oxidizing (H_2O/Ar) atmosphere. Before switching from reduction to oxidation atmospheres and *vice versa*, the remaining reactive gases were removed by an argon flush flow for 5 min.

For the reduction step, different H_2/Ar flowrates (2, 3.4 and 5% v) were used. The duration of this step was determined in order to achieve a complete reduction of $NiWO_4$ to Ni and W, *i.e.*, 20.9% of theoretical weight loss.

For the reoxidation of the sample, a mixture of steam and argon was supplied by a water temperature-controlled saturator using an Ar flow, with concentrations of 0.8, 1.5 and 2.2% v H_2O/Ar. The duration of this step was established in order to complete the full reoxidation of Ni and W back to $NiWO_4$ (until no mass change could be detected).

Based on TGA results according to experimental conditions of Table 1, global kinetic parameters such as initial reaction rates, reaction constants and orders, as well as activation energies for the reduction and oxidation steps were calculated.

Hydrogen storage multicycle stability test

It is important to point out the importance of the thermal stability of the materials used to storage hydrogen in CL operation, because the materials employed in this process are expected to be exposed to multiple (redox cycles) absorption and release of hydrogen. Therefore, a multi-cycle redox test was performed with the purpose of testing the thermal stability of $NiWO_4$. This was evaluated by exposing the sample to seventeen consecutive redox cycles and comparing the weight change progress of each cycle as function of time at a constant temperature of 800 °C using 5% v H_2/Ar and 2.2% v H_2O/Ar as reducing and oxidizing gases, respectively.

Results and discussion

Thermodynamic analysis

Fig. 1 shows the sensitivity analysis of $NiWO_4$ formation as function of reactor temperature and H_2O molar feed in combination with 1 kmol h^{-1} of W and Ni each to a Gibbs reactor using Aspen Plus process simulator. In this figure, it is possible to observe the conditions for full regeneration to $NiWO_4$, which according to the results is a window with

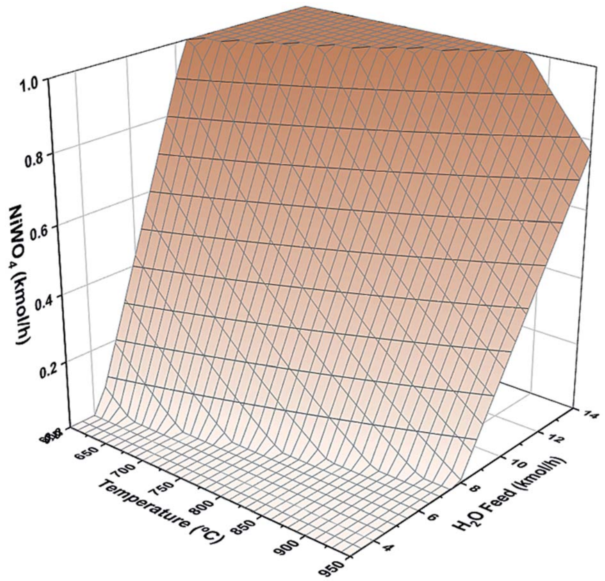

Fig. 1 Thermodynamic analysis surface response of molar $NiWO_4$ formation in regeneration step.

temperatures from 600 to 870 °C and H_2O molar flow rates from 6.5 to 13.5 kmol h^{-1}, respectively.

Hydrogen storage performance evaluation

Fig. 2 shows a synthetized $NiWO_4$ sample evaluated for a hydrogen storage performance at different stages of reduction and oxidation using TGA at 800 °C. In this figure theoretical weight changes of $NiWO_4$ and reduced Ni + W species are represented by horizontal lines corresponding to 100% w (orange) and 79.1% w (green), respectively. Fig. 2(a) starts with the fresh synthetized $NiWO_4$ sample corresponding to a 100% w, while Fig. 2(b) shows the first reduction of this material, which achieved a complete reduction using 5% v H_2 (R-sample), since this reached the theoretical Ni + W% w. After this, the sample was oxidized using 2.2% v H_2O/Ar. Fig. 2(c) shows the sample weight change at an intermediate oxidation stage (TGA, 93% w) between the fully reduced and oxidized steps. Furthermore, Fig. 2(d) illustrates the sample reaching the total % w corresponding to the complete theoretical oxidation to $NiWO_4$, using the same oxidation conditions that started at point 2(b) (RO-sample). In addition, Fig. 2(e) indicates that the reduced sample reached again the fully reduced species (Ni + W), corresponding to the second cycle performed at the same reducing conditions previously employed (ROR-sample). Finally, Fig. 2(f) identifies the final oxidation step after 17 consecutive redox cycles, reaching again the % w corresponding to the fully $NiWO_4$ oxidized specie.

Characterization

XRD. Fig. 3(a) shows the XRD pattern of the synthesized material. This diffractogram corresponds to the crystallographic phase of nickel tungstate ($NiWO_4$) in agreement with the ICSD collection code 015852.[52] Furthermore, Fig. 3(b) presents the diffractogram obtained from reduced $NiWO_4$ under 5% v H_2/Ar atmosphere in a TGA (Fig. 2(b)). Here it is clearly observed that Ni and W are the only metallic species being present, which indicate a complete reduction of nickel tungstate. These results are consistent with studies reported elsewhere.[50,53] On the other hand, Fig. 3(c) shows the diffractogram of the intermediate TGA weight change (93% w) between the reduced sample and oxidation using 2.2% v H_2O/Ar corresponding to Fig. 2(c). In this diffractogram it is evident the presence of WO_2 as an intermediate specie along with Ni and $NiWO_4$ in the process towards the total reoxidation to $NiWO_4$. At this stage, it is important to notice that metallic Ni is not thermodynamically possible to be oxidized with steam towards NiO.[47] Furthermore, Fig. 3(d) shows the XRD pattern of the sample after being exposed to seventeen redox cycles in a TGA (Fig. 2(f)).

According to this diffractogram (Fig. 3(d)), the only crystallographic phase obtained agreed with the nickel tungstate

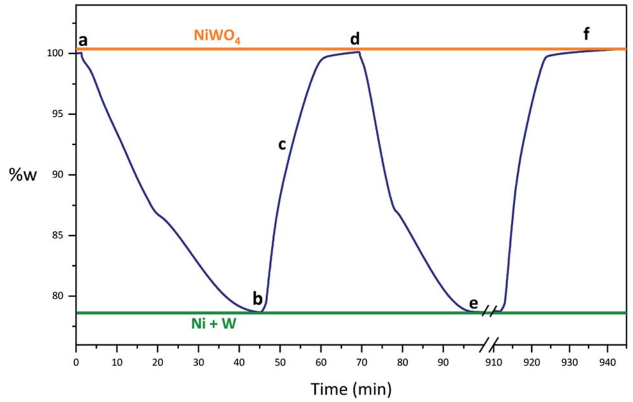

Fig. 2 TGA hydrogen-storage performance evaluation at different stages of reactions.

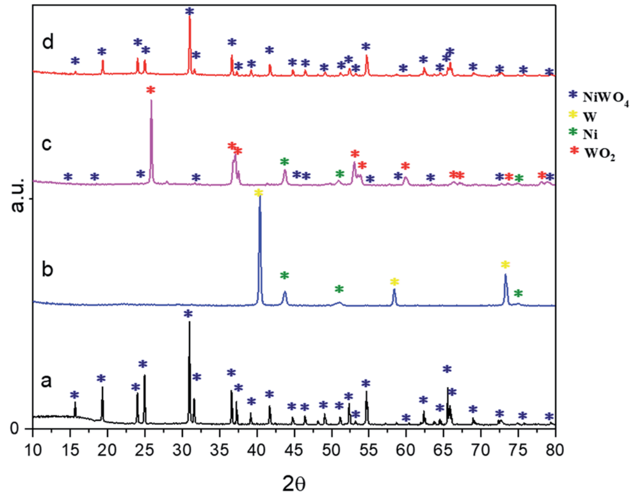

Fig. 3 XRD patterns of the fresh synthesized sample (a), complete reduction (b), half-way oxidized (c), and complete oxidation after 17 TGA redox cycles (d).

structure, ICSD collection code 015852, which corresponds to the same crystallographic phase found at the beginning of the redox cycles (fresh sample).

Based on results from XRD diffractograms Fig. 3(c) and (d) it is proposed that the reaction path that explains these results are as follows:

$$W + 2H_2O \rightarrow WO_2 + 2H_2 \quad (5)$$

$$Ni + WO_2 + 2H_2O \rightarrow NiO\cdot WO_3 + 2H_2 \quad (6)$$

First, W is oxidized to WO_2 according to reaction (5) and secondly, Ni and WO_2 are oxidized by steam according to the gas–solid reaction (6). It is important to note that previously formed tungsten dioxide (WO_2) reacts along with Ni through a gas–solid reaction with H_2O, this last providing the required oxygen for the formation of $NiWO_4$. Furthermore, one way to explain these results can be based on the fact that presumably the inclusion of Ni in the crystal lattice of tungsten dioxide (WO_2) inhibits the formation of the WO_3 phase during its oxidation with water vapor. This simultaneously favors the formation of nickel tungstate ($NiO*WO_3$ or $NiWO_4$) phase when is further oxidized, which is consequently the final phase found according to the X-ray diffraction results reported in Fig. 3(d). The latter is because it is thermodynamically impossible to oxidize Ni with steam as indicated in the thermodynamic analysis section. Therefore, the only source of oxygen capable of oxidizing W + Ni must be through a reaction path that involved the formation of WO_2 as an intermediate specie, which is consistent with results from XRD characterization leading to the overall regeneration reaction (4).

BET surface area. Moreover, BET analysis of the fresh $NiWO_4$ sample indicates a surface area of 4.25 $m^2\ g^{-1}$, which agrees with results found by Quintana *et al.*[54] who reported a range of BET surface areas between 16 to 3 $m^2\ g^{-1}$ produced by the precipitation method and calcined at 400 and 800 °C, respectively. Due to the small amount of sample employed during the TGA tests (20 mg) it was not possible to perform BET analysis of other samples produced during the TGA test.

SEM and EDS analysis. Fig. 4 presents SEM images of the $NiWO_4$ sample at different steps described in the TGA test presented in Fig. 2. In Fig. 4(a) it can be observed that fresh $NiWO_4$ sample is composed of non-porous (rock-like) large particles of polygonal morphologies with sizes varying between 1 and 5 μm and similar to those reported by Quintana *et al.*[54] Fig. 4(b1 and b2) shows the same sample after the first reduction according to TGA Fig. 2(b) (R-sample). In this image it can be observed how the initial particle changed its surface morphology from a non-porous rock-like regular shape to a porous coral-like morphology formed by a network of particle agglomerates of about 50 nm size (see ESI†) with cavities between 50 to 100 nm size. These morphologies have been observed previously by Tatsumi *et al.*[55] for $NiO–NiFe_2O_4$ and Ahmed *et al.*[56] for $NiWO_4$ calcined in a temperature range from 750 to 900 °C. According to these authors and Kang and Jeong,[53] the reduction process is as follows:

$$NiWO_4 + H_2 \rightarrow Ni + WO_3 + H_2O \quad (7)$$

$$WO_3 + H_2 \rightarrow WO_2 + H_2O \quad (8)$$

$$WO_2 + H_2 \rightarrow W + H_2O \quad (9)$$

However, no attempt has been made to explain the formation of the resulting solid porous morphology after the reduction process of $NiWO_4$ with H_2.

Fig. 5 shows a representation of a proposed reduction process to explain the obtained morphology. First, it starts with a solid non-porous $NiWO_4$ particle, which according to reaction (7) leads to the formation of Ni particles surrounding and enclosing WO_3 particles (1st stage). These WO_3 species enclosed by Ni particles can be explained in terms of results from a research conducted by Inomata *et al.*,[57] who showed that the solid-state diffusion between W and Ni in a similar range of temperatures (as used in the present research) is mainly controlled by boundary and volume diffusion. According to Fig. 5, Ni formed in the first stage prevents shrinkage of the resulting material, whilst W formed species begin to diffuse through Ni and the formation of inner particles of W species surrounded by Ni particles take place. They called this phenomenon a diffusion induced recrystallization (DIF) that predominantly produce W species into Ni by volume diffusion, which is enhanced by the high diffusivity of W in Ni ($D = 9.2 \times 10^{-18}\ m^2\ s^{-1}$ at $T = 800$ °C) where initial pores are formed due to the reduction of NiO to Ni. However, WO_3 is still not reduced and the size of the original $NiWO_4$ particles can be maintained during this first reduction reaction. In the second reduction step (2nd stage), WO_3 is reduced to WO_2, with the consequent release of gaseous water according to reaction (8). This gas generation causes pores to form because of its escape from the inner to the outer solid structure of the material. Finally, WO_2 is further reduced by H_2 (3rd stage) according to reaction (9), thus generating additional porosity due to the release of H_2O according to this reaction and forming species Ni + W as overall reduction products. This generating a coral-like morphology and a network of porous structure, which will be crucial for explaining the fast steam-oxidation kinetics observed in the kinetic section of this paper.

Fig. 4(c) shows an SEM image of the sample after one complete redox cycle (RO-sample) using 5% v H_2/Ar and 2.2% v H_2O/Ar during reduction and oxidation steps, respectively. Here it can be observed a different morphology compared to the fresh sample of Fig. 4(a), in this image, clusters of particle agglomerates are observed and this can be explained in terms of the high temperature exposure of the sample (800 °C). However, particle sizes were reduced from 1–5 μm from the fresh sample to 0.2–1 μm, this caused by the oxidation of the porous network of particles, thus producing smaller particles forming clusters of agglomerates.

On the other hand, Fig. 4(d) shows the SEM image of the sample after a second reduction (ROR-sample, spot d in TGA test) where it can be observed that a similar structure to Fig. 4(b1 and b2) was produced, but containing larger porous

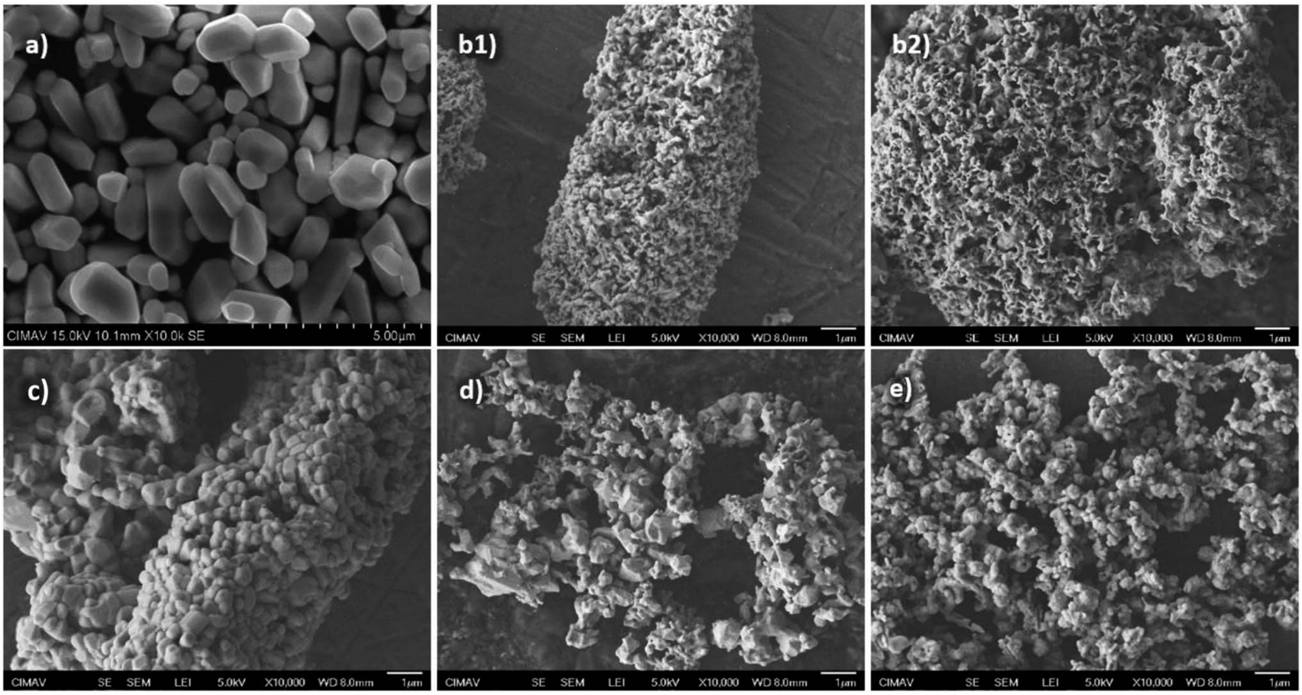

Fig. 4 SEM images of the fresh sample (a), R-sample (b1 and b2), RO-sample (c), ROR-sample (d) and oxidized sample after 17 consecutive redox cycles (e).

within the particles. This behavior can be explained because, unlike in the first reduction, here the reduction starts with smaller initial particles. This is consistent from this cycle onwards, which is confirmed by the morphology of the oxidized sample after 17 redox cycles shown in Fig. 4(e).

In summary, after the first cycle, the most significant change in the sample was its morphology that suffered important changes as shown in Fig. 4(b1 and b2) (first reduction SEM images) and Fig. 4(c) (first cycle oxidation). The morphology of the oxidized sample after the first cycle is clearly not the same as the fresh $NiWO_4$ sample (Fig. 4(a)). However, the morphology of the oxidized sample at the beginning of the second cycle (Fig. 4(c)) and after the reduction during the second cycle (Fig. 4(d)) is very alike to the morphology of the sample after

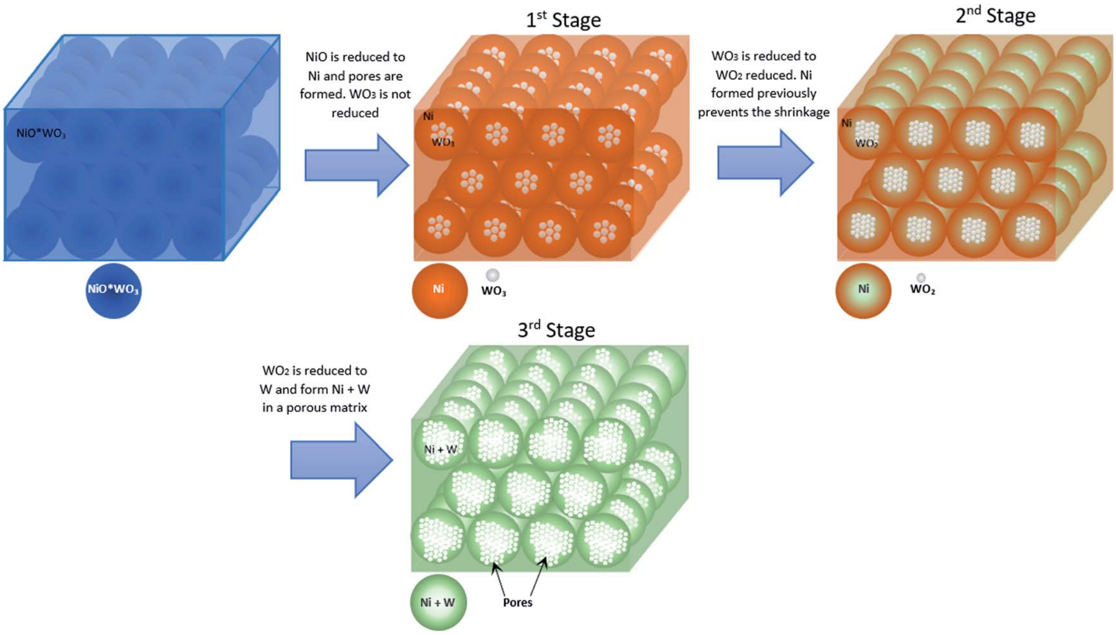

Fig. 5 Schematic image for the transformation of $NiWO_4$ to a porous Ni + W specie.

seventeen cycles (Fig. 4(e)). The reason why a comparison in terms of characterization results was made between the second and after seventeen cycles obeys to the fact that after the second cycle the material is consistent in terms of morphology and this is a key feature in the behavior of the material under cyclic operation. This behavior indicates that after the first cycle the material begins to adapt to the reaction cycling conditions and reaches its reaction and thermal stability, since after this second cycle and beyond (17 consecutive cycles) no significant difference in terms of reactivity, composition and morphology was observed. This was reflected in the corresponding characterization (XRD, SEM and EDS analyses) results obtained after seventeen consecutive cycles, which established the $NiWO_4$ stability.

Table 2 shows results from EDS analysis of the fresh sample (a), first reduced sample (b), first oxidized sample (d), second reduced sample (e) and the oxidized sample after 17 consecutive redox cycles (f). EDS images also are reported in Fig. S3 of ESI.† Elemental composition values from Table 2 of the fresh sample are consistent with the theoretical composition of $NiWO_4$. On the other hand, the (b) sample, which theoretically should be composed only by Ni and W presents traces of oxygen (1.96% w). This is possibly due to the oxidation that takes place between the sample and the environmental air during vialing and handling this sample to different analyses.

Furthermore, column (d) shows the elemental composition of the sample after being oxidized under steam and completing the first redox cycle. This composition is very similar to the theoretical values of $NiWO_4$. This result confirms that $NiWO_4$ was fully regenerated after the oxidation reaction and agrees well with results from the TGA test and XRD analysis.

Likewise, column (e) confirms the elemental composition reached in a second reduction with hydrogen, which again is very close to the theoretical Ni + W composition. While column (f) shows that the sample returns to a composition close to the theoretical $NiWO_4$ values after completing 17 redox cycles, thus showing the high thermal stability of this material. From this table it can be seen that there is a good agreement between the proposed reaction steps and results from EDS, TGA and XRD analyses previously described.

Global kinetic study. From the TGA signal response in Fig. 2, the slope obtained ($\Delta w/\Delta t$) is proportional to the initial reaction rate ($-r_A$). Initial reaction rates were evaluated for each one of the 17 tests that were previously described in Table 1.

According to what is widely known, this reaction can be studied by a usual model of a gas–solid reaction rate according to the following expression:[58]

$$-r_A = kC_A{}^n \tag{10}$$

where k is the reaction rate constant, n is the reaction order with respect to reactant gas and C_A is the H_2 or H_2O concentrations in mol fraction for the reduction or oxidation steps, respectively.

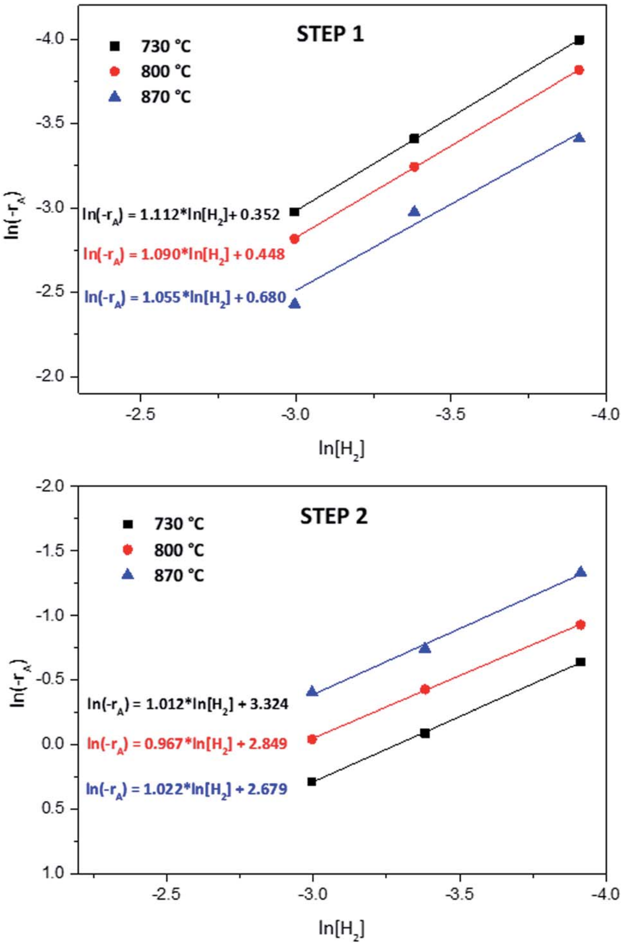

Fig. 6 Reaction order plots for the first and second reduction steps of $NiWO_4$ respect to H_2 concentration.

Table 2 EDS results of the fresh sample (a), R-sample (b), RO-sample (d), ROR-sample (e) and the sample after 17 consecutive redox cycles (f)

Elemental composition (% w)							
Element	(a)	(b)	(d)	(e)	(f)	Theoretical oxidized sample	Theoretical reduced sample
O	22.49	1.96	25.22	3.19	23.00	25.21	0.00
W	59.05	70.34	55.73	70.00	57.10	56.49	75.80
Ni	18.46	27.70	19.05	26.81	19.90	18.30	24.20

Reduction kinetics. The global reaction order for the $NiWO_4$ reduction with respect to the hydrogen concentration at experimental conditions previously described is shown in Fig. 6. The logarithm of the reaction rate *vs.* the logarithm of the hydrogen concentration is plotted in this figure. A linear equation results from the analysis at each temperature condition, where the ordinate axis intersect represents the logarithm of the reaction rate constant (k) and the slope (n) the reaction order at a specific temperature.

By a careful observation of the TGA response from Fig. 2 during the $NiWO_4$ reduction, a change of slope is evident, which is related to different reactions that take place in this process. According to and Kang and Jeong,[53] Ahmed[56] and Sidhar[59] the reduction of $NiWO_4$ kinetics is reported to occur in two steps. The initial step is associated to the reduction of NiO to Ni as indicated in reaction (7) while W species remain in its oxidation state as WO_3. During the second step of the kinetics, WO_3 is reduced to WO_2 and this is further reduced to W according to reactions (8) and (9). Therefore, a kinetic evaluation of these two steps was made in order to determine global kinetic parameters (reaction order, reaction constants, and activation energies).

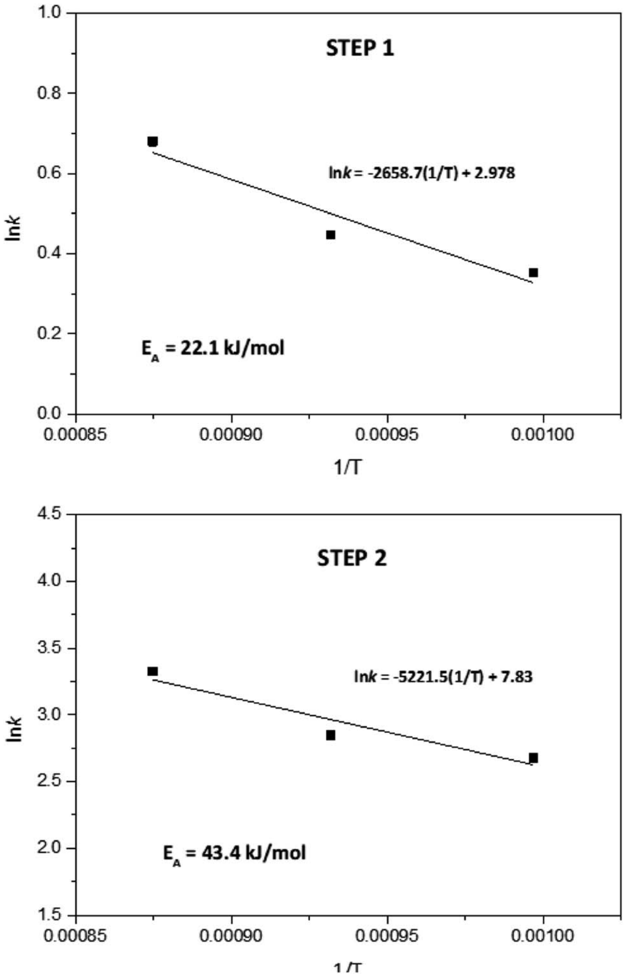

Fig. 7 Arrhenius plots for the reduction steps.

According to results from Fig. 6, for the first reduction step (step 1), the reaction order varied between 1.05 and 1.11. Therefore, it can be concluded that the global reduction reaction of $NiWO_4$ to Ni + WO_2 is first order with respect to the hydrogen concentration. Furthermore, the second step reduction from Ni + WO_2 to Ni + W presents a reaction order that varied from 0.97 to 1.02, which represents also a global first order reaction with respect to the H_2 concentration. By using the k values generated in Fig. 6, Arrhenius plots for each reduction step can be calculated and these are presented in Fig. 7. From these plots, it can be observed that activation energies for the reduction of $NiWO_4$ during step 1 and 2 are 22.11 and 43.41 kJ mol^{-1}, respectively. These values agree well with those found by Ahmed *et al.*, who reported activation energies of 18 and 38 kJ mol^{-1} for these two steps, respectively. It is important to indicate that most of the previous kinetic studies performed on the reduction of $NiWO_4$ do not report the influence of the H_2 concentration as the present study does. Li *et al.*[5] recently reported several ferrite-spinel materials for hydrogen storage using hydrogen and steam during reduction and oxidation, respectively. They found hydrogen reduction global activation energies in a temperature range from 450 to 850 °C for Fe_3O_4 (E_A = 98.63 kJ mol^{-1}), $Zn_{0.25}Fe_{2.75}O_4$ (E_A = 86.67 kJ mol^{-1}), $Mn_{0.25}Fe_{2.75}O_4$ (E_A = 76.31 kJ mol^{-1}), $Cu_{0.25}Fe_{2.75}O_4$ (E_A = 52.05 kJ mol^{-1}), $Ni_{0.25}Fe_{2.75}O_4$ (E_A = 45.36 kJ mol^{-1}) and $Co_{0.25}Fe_{2.75}O_4$ (E_A = 35.36 kJ mol^{-1}). By comparing these values with the global activation energies for steps 1 and 2 of $NiWO_4$ reduction with hydrogen, it can be seen that lower activation energies are needed for nickel tungstate than those recently reported in the literature for mixed oxides under similar conditions, which confirms the potential of $NiWO_4$ in hydrogen storage applications.

Oxidation kinetics. According to results from Fig. 2, is can be seen that the oxidation of the reduced metallic species (Ni + W) occurs in a fast single straight line that covers almost the entire oxidation process (*ca.* 99% w). The remaining 1% w can be attributed to difusional limitations of H_2O molecules to reach

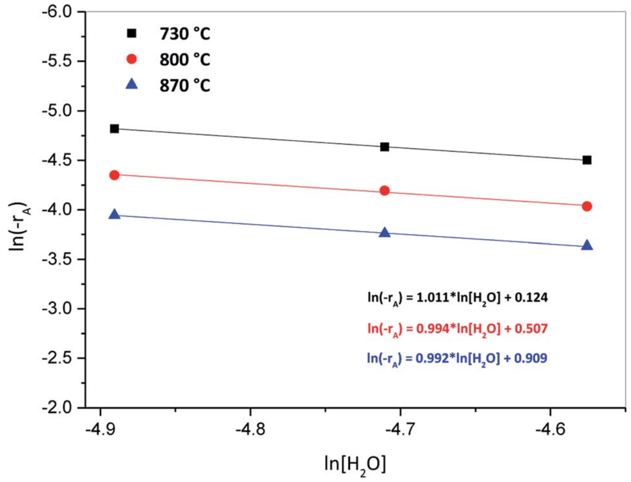

Fig. 8 Reaction order plot for the oxidation step of $NiWO_4$ respect to H_2O concentration.

a small portion of the unreacted reduced species. Therefore, the kinetic analysis of the oxidation step was made by taking into account the main oxidation reaction process (reaction (4)).

Fig. 8, presents results of a plot of ln[H_2O] *vs.* ln($-r_A$) for the three oxidation temperatures of 730, 800 and 870 °C, where the slope of each line represents the reaction order and the intercept with the *y* axis the reaction constant at each temperature. According to results from this figure, the reaction order varied from 0.99 to 1.08, which represents a global reaction order of one with respect to the H_2O concentration, whereas the reaction constants were 0.053, 0.074 and 0.102 s^{-1} for 730, 800 and 870 °C, respectively.

Furthermore, Fig. 9 presents the Arrhenius plot for the oxidation step. In the case of steam oxidation reaction, the global activation energy obtained was 53.4 kJ mol^{-1}. Here, it is important to indicate that according to XRD results of the oxidation process presented previously, the mechanism identified for the oxidation of Ni + W back to $NiWO_4$ starts with W being oxidized by steam to form WO_2 and H_2 (reaction (5)) and in a second step Ni, WO_2 and H_2O simultaneously react to form $NiWO_4 + H_2$ (reaction (6)). This means that during the oxidation process WO_3 was not formed as an intermediate specie. This behavior is consistent with previous studies performed by Wendel[60] and Smolik *et al.*[61,62] that described the oxidation of W with H_2O as follows:

$$W + 2H_2O \rightarrow WO_{2(s)} + 2H_{2(g)} \tag{11}$$

$$WO_{2(s)} + 2H_2O \rightarrow WO_3^*H_2O_{(g)} + H_{2(g)} \tag{12}$$

They have found that the formation of gaseous specie $WO_3^*H_2O$ leads to the sublimation of W an ultimately to the loss of W under steam atmospheres in a temperature range between 200 to 1100 °C. Furthermore, Sabourin and Yetter[63] performed the oxidation of W with a mixture of steam and H_2 in order to inhibit the formation of W volatile species an consequently the loss of tungsten.

The facts that all W was reacted with Ni and H_2O to form $NiWO_4$ and that no loss of W was found during the TGA tests corroborates that WO_3 is not an intermediate during the oxidation step and that the formation on $NiWO_4$ prevents the volatilization of W in the present research. Furthermore, activation energy for the oxidation of W with steam has been reported to be 129 and 139 kJ mol^{-1} according to Smolik *et al.*,[61,62] which is 2.6 times greater than the activation energy reported in Fig. 9, this is presumably attributed to the presence of Ni during the oxidation process and to the unique coral-like morphology of W + Ni that presents an interparticle porous network as seen in SEM Fig. 4(b2). This particular morphology presumably eases the diffusion of reactant gaseous H_2O, thus increasing Ni + W oxidation kinetics. A further modeling kinetic study would be needed in order to determine the intrinsic activation energy and possible mass transport and/or diffusional limitations during the oxidation step, however, this study is out of the scope of the present investigation.

Finally, according to results obtained in this research, the global kinetic expressions for the reduction (steps 1 and 2) and oxidation reactions are respectively as follows:

$$-r_1[NiWO_4] = 2.98e^{\left(-\frac{22.1}{RT}\right)}y_{H_2} \tag{13}$$

$$-r_2[NiWO_4] = 7.83e^{\left(-\frac{43.4}{RT}\right)}y_{H_2} \tag{14}$$

$$-r[Ni + W] = 6.51e^{\left(-\frac{53.4}{RT}\right)}y_{H_2O} \tag{15}$$

Hydrogen storage multicycle stability test. A multicycle thermal stability test was carried out by TGA and this is presented in Fig. 10. Weight loss by reduction and weight gain by oxidation was in average approximately equal to 20.7% w compared with the theoretical 20.9% w, which corresponds to the weight change from $NiWO_4$ to Ni + W species. Results obtained clearly show that the material presents a significant

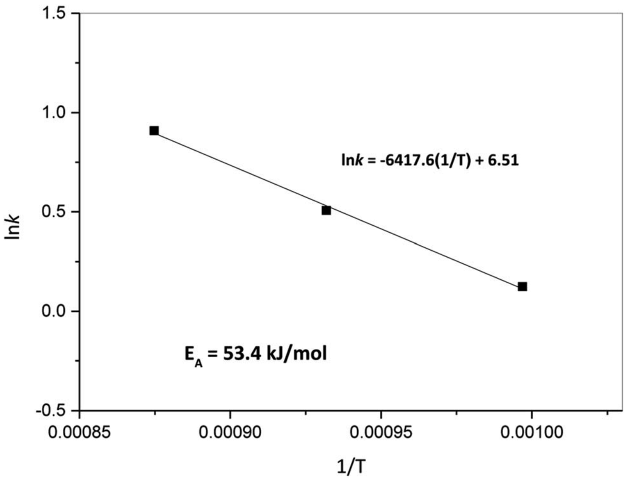

Fig. 9 Arrhenius plot for the oxidation step.

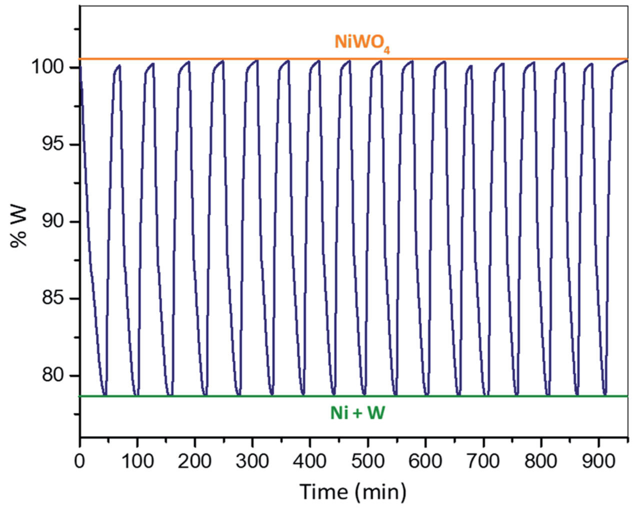

Fig. 10 $NiWO_4$ multicycle thermal stability TGA test.

thermal stability during the seventeen-hydrogen storage-release cycles, where no apparent deactivation is observed by comparing the % w difference between the first and last cycles. Furthermore, XRD and EDS results from Fig. 3(d) and Table 2, respectively, confirm that the sample composition obtained after seventeen consecutive cycles is the same as the initial $NiWO_4$, which demonstrates the high stability of the sample under the exposed conditions.

By comparing the present results to other materials reported in the literature under similar multicycle tests it can be assessed the potential of $NiWO_4$ for hydrogen storage through a CL operating scheme. Lorente *et al.*[64] studied the effect of added metals Al, Cr and Ce to Fe_2O_3 in the steam-iron process. They reported an improvement in the thermal stability and oxidation activity of the solids during seven consecutive redox cycles. However, their materials showed a reduction in hydrogen storage capacity between 7 to 16% w according to the type of additive used, while no key information related to the reduction and oxidation kinetics was reported. In another research using a ternary ferrite-spinel ($Cu_{0.5}Co_{0.5}Fe_2O_4$) reported by Zeng *et al.*,[65] they found that the hydrogen storage performance was maintained with only negligible deactivation being observed after twenty consecutive redox cycles. This behavior compares well with the stability exhibited by other similar hydrogen storage materials containing rare earths. However, their material presents only a theoretical volumetric hydrogen storage density (VSD) of 65.58 g L^{-1} compared to a high VSD of 496 g L^{-1} of $NiWO_4$. Furthermore, Zeng *et al.*[35] studied a $CoFeAlO_x$ spinel material, which was exposed to twenty CO–H_2O redox cycles at 800 °C. They found a significant deactivation of this material. Nevertheless, their reduction lasted for 90 minutes ($r_{red} = 0.16\%$ w min^{-1}) and the oxidation was completed after 60 minutes ($r_{oxi} = 0.25\%$ w min^{-1}), which corresponds to the kinetics of this material. However, they did not evaluate the global kinetics of this material based on an activation energy. In another recent research, Fe_2MnO_4 was exposed to a redox cycle at 775 °C using 5% v H_2/Ar and 2% v H_2O/Ar during the reduction and oxidation, respectively.[51] However, the redox kinetics of this material was not studied, but the oxidation lasted for 73 minutes with a $r_{oxi} = 0.28\%$ w min^{-1}. Huang *et al.*[66] studied the $NiFe_2O_4$ oxygen carrier under a water-splitting CL reaction scheme. They subjected this material to CO–H_2O redox cycles and found that the reduction of $NiFe_2O_4$ was 19.61% w at 790 °C, while its reduction time lasted 60 min ($r_{red} = 0.36\%$ w min^{-1}); however, oxidation with steam needed 130 min ($r_{oxi} = 0.15\%$ w min^{-1}) to be achieved. Comparing TGA results from $NiWO_4$ as a hydrogen storage material with above results reported in the literature, it is possible to observe (Fig. 10, a redox TGA weight change of 20.7% w at 800 °C) that the reduction time lasted 30 minutes ($r_{red} = 0.69\%$ w min^{-1}) while oxidation under steam took 20 minutes ($r_{oxi} = 1.03\%$ w min^{-1}). Therefore, it can be concluded from the above comparison that $NiWO_4$ exhibits a superior behavior in terms of reducibility, hydrogen storage capacity and reduction–oxidation kinetics. Furthermore, Li *et al.*[5] recently reported multicycle stability tests for ferrite-spinel materials under hydrogen reduction and steam oxidation during 10 redox cycles at 550 °C. They found a percentage reduction (%) in hydrogen storage capacity after 10 cycles for Fe_3O_4 (33%), $Zn_{0.25}Fe_{2.75}O_4$ (24%), $Mn_{0.25}Fe_{2.75}O_4$ (15%), $Cu_{0.25}Fe_{2.75}O_4$ (13%), $Ni_{0.25}Fe_{2.75}O_4$ (11%) and $Co_{0.25}Fe_{2.75}O_4$ (2%). Whereas the percentage reduction for $NiWO_4$ after 17 redox cycles (Fig. 10) at a higher temperature of 800 °C was negligible. This significant result confirms the high multicycle redox thermal stability of $NiWO_4$ for hydrogen storage applications.

Conclusions

$NiWO_4$ with a volumetric storage density (VSD) of 496 g L^{-1} was studied to evaluate its feasibility as a hydrogen storage material under a CL reaction scheme using hydrogen and steam during its reduction and oxidation steps, respectively. The material was synthesized by precipitation and calcined at 950 °C for 5 hours in air. Characterization consisted in XRD, BET surface area, SEM and EDS analysis. A thermodynamic analysis was performed to explore oxidation conditions of $NiWO_4$ reduced species (Ni + W). $NiWO_4$ hydrogen storage evaluation was performed by TGA using 5% v H_2/Ar and 2.2% v H_2O/Ar at 800 °C. Global kinetics for the reduction step was studied in a temperature range from 730 to 870 °C using 2 to 5% v of H_2/Ar. While oxidation kinetics was examined from 730 to 870 °C using 0.8 to 2.2% v H_2O/Ar. Finally, a hydrogen storage multicycle stability test was performed by exposing $NiWO_4$ to seventeen consecutive redox cycles. XRD results indicate that $NiWO_4$ was the only crystalline phase obtained of the synthesized material. Fully reduced material consisted of only W and Ni species, while reoxidation led back to $NiWO_4$ specie. Furthermore, XRD results also helped to propose a reaction path for the oxidation of Ni + W species to form $NiWO_4$. BET surface area of the synthesized material was 4.25 m^2 g^{-1}. SEM results showed that fresh $NiWO_4$ was composed of non-porous (rock-like) large particles of polygonal morphologies with sizes varying between 1 and 5 μm. After the reduction step, the reduced species changed to a porous coral-like morphology formed by a network of particle agglomerates of about 50 nm size with cavities between 50 to 100 nm size. A reduction process was proposed based on SEM images to explain the drastic morphology changes observed during the reduction step in terms of a solid-state diffusion phenomenon between W and Ni, which presumably prevents the shrinkage of the resulting material leading to a porous material. EDS analysis results confirmed the compositions of the reduced (Ni + W) and fully oxidized $NiWO_4$ species, respectively. Global kinetic studies indicate a first order reaction for the first and second steps during reduction of the material ($n = 1$), while a reaction order of $n = 1$ for the oxidation, with activation energies of 22.1, 48.4 and 53.4 kJ mol^{-1} for the two reduction and oxidation steps, respectively. $NiWO_4$ multicycle stability test shown no loss of VSD and fast reduction and oxidation kinetics under the studied conditions after seventeen consecutive redox cycles, which confirms the potential of this material with respect to current oxygen carriers reported in the literature for hydrogen storage applications.

Finally, the proof of concept of $NiWO_4$ as an oxygen carrier employed for hydrogen storage under a CL operating reaction scheme completed in the present research (synthesis, characterization, TGA evaluation and reaction kinetics), will set the foundations for future studies in this field. These studies should focus on the use of a greater amount of sample along with another experimental configuration such as fixed or fluidized bed reactors. Particle size and attrition resistance (mechanical strength) during a cycling reaction scheme play important roles to evaluate the suitability of this material under CL operation as well as the concentration of the product gases generated in each step and ultimately, a process simulation effort to evaluate the mass and energy balances in a hydrogen storage chemical looping reaction system. All the previous aspects of CL operation need to be determined in order to assess the feasibility of $NiWO_4$ towards its industrial application as an oxygen carrier towards a more realistic evaluation of this material will be the matter of upcoming endeavors of our research group.

Author contributions

P. E. González-Vargas: writing – original draft, writing – review & editing and investigation; J. M. Salinas-Gutiérrez: formal analysis; M. J. Meléndez-Zaragoza: formal analysis; J. C. Pantoja-Espinoza: data curation and supervision; V. Collins-Martínez: investigation, methodology and supervision; A. López-Ortiz: writing – original draft, writing – review & editing, investigation, supervision and project administration.

Conflicts of interest

There are no conflicts to declare.

Acknowledgements

Authors are grateful to Ernesto Guerrero Lestarjette and Pedro Pizá Ruiz for the XRD analysis and interpretation of powder samples, to Luis de la Torre for the BET surface area analysis, to Karla Campos for the SEM and EDS analysis and to the national laboratory of nanotechnology, Nanotech from CIMAV. Authors also are thankful to CONACYT for the scholarship awarded to the student involved in the project.

Notes and references

1 A. Sunny, P. A. Solomon and K. Aparna, *J. Nat. Gas Sci. Eng.*, 2016, **30**, 176–181.

2 T. De Los Ríos, V. Collins Martinez, M. D. Delgado Vigil and A. López Ortiz, *Int. J. Chem. React. Eng.*, 2007, **5**(A30), 1–12.

3 V. Collins-Martinez, M. Escobedo Bretado, M. Meléndez Zaragoza, J. Salinas Gutiérrez and A. L. Ortiz, *Int. J. Hydrogen Energy*, 2013, **38**, 12539–12553.

4 T. da Silva Veras, T. S. Mozer, D. da Costa Rubim Messeder dos Santos and A. da Silva César, *Int. J. Hydrogen Energy*, 2017, **42**, 2018–2033.

5 M. Li, Y. Qiu, L. Ma, D. Cui, S. Zhang, D. Zeng and R. Xiao, *Sustainable Energy Fuels*, 2020, **4**, 1665–1673.

6 M. S. El-Eskandarany, *RSC Adv.*, 2019, **9**, 9907–9930.

7 S. M. Aceves, G. D. Berry, J. Martinez-Frias and F. Espinosa-Loza, *Int. J. Hydrogen Energy*, 2006, **31**, 2274–2283.

8 Z. Ma, R. Xiao and H. Zhang, *Energy Technol.*, 2017, **5**, 1399–1406.

9 U. Eberle, M. Felderhoff and F. Schüth, *Angew. Chem., Int. Ed.*, 2009, **48**, 6608–6630.

10 S. Niaz, T. Manzoor and A. H. Pandith, *Renewable Sustainable Energy Rev.*, 2015, **50**, 457–469.

11 B. Jiang, B. Dou, Y. Song, C. Zhang, B. Du, H. Chen, C. Wang and Y. Xu, *Chem. Eng. J.*, 2015, **280**, 459–467.

12 T. De Los Ríos-Castillo, *Óxidos Metálicos Mixtos Como Portadores De Oxígeno Para Procesos Redox a Partir De Metano*, 2010.

13 V. Hacker, R. Vallant and M. Thaler, *Ind. Eng. Chem. Res.*, 2007, **46**, 8993–8999.

14 W. Hui, S. Takenaka and K. Otsuka, *Int. J. Hydrogen Energy*, 2006, **31**, 1732–1746.

15 H. S. Kim, K. S. Cha, B. K. Yoo, T. G. Ryu, Y. S. Lee, C. S. Park and Y. H. Kim, *J. Ind. Eng. Chem.*, 2010, **16**, 81–86.

16 H.-S. Kim, D.-H. Lee, H.-S. Kim, C.-S. Park and Y.-H. Kim, *J. Nanomater.*, 2013, **2013**, 1–7.

17 Y. H. Kim, H. S. Je, E. J. Kang, S. G. Lee and C. S. Park, *Adv. Mater. Res.*, 2011, **347–353**, 3317–3320.

18 Y. H. Kim, E. J. Kang, S. G. Lee, H. S. Kim and C. S. Park, *Adv. Mater. Res.*, 2012, **554–556**, 616–619.

19 O. Mihai, D. Chen and A. Holmen, *Ind. Eng. Chem. Res.*, 2011, **50**, 2613–2621.

20 M. Rydén, H. Leion, T. Mattisson and A. Lyngfelt, *Appl. Energy*, 2014, **113**, 1924–1932.

21 G. L. Schwebel, S. Sundqvist, W. Krumm and H. Leion, *Elsevier*, 2014, **2**, 1131–1141.

22 D. Zeng, Y. Qiu, S. Peng, C. Chen, J. Zeng, S. Zhang and R. Xiao, *J. Mater. Chem. A*, 2018, **6**, 11306–11316.

23 M. Liao, Y. Chen, Z. Cheng, C. Wang, X. Luo, E. Bu, Z. Jiang, B. Liang, R. Shu and Q. Song, *Appl. Energy*, 2019, **252**, 113435.

24 B. Dou, H. Zhang, Y. Song, L. Zhao, B. Jiang, M. He, C. Ruan, H. Chen and Y. Xu, *Sustainable Energy Fuels*, 2019, **3**, 314–342.

25 K. Otsuka, C. Yamada, T. Kaburagi and S. Takenaka, *Int. J. Hydrogen Energy*, 2003, **28**, 335–342.

26 S. Takenaka, V. T. Dinh Son and K. Otsuka, *Energy Fuels*, 2004, **18**, 820–829.

27 A. Shafiefarhood, J. C. Hamill, L. M. Neal and F. Li, *Phys. Chem. Chem. Phys.*, 2015, **17**, 31297–31307.

28 V. Fleischer, R. Steuer, S. Parishan and R. Schomäcker, *J. Catal.*, 2016, **341**, 91–103.

29 S. Chen, L. Zeng, H. Tian, X. Li and J. Gong, *ACS Catal.*, 2017, **7**, 3548–3559.

30 A. Löfberg, J. Guerrero-Caballero, T. Kane, A. Rubbens and L. Jalowiecki-Duhamel, *Appl. Catal., B*, 2017, **212**, 159–174.

31 S. Ma, S. Chen, Z. Zhao, A. Soomro, M. Zhu, J. Hu, M. Wu and W. Xiang, *Energy Fuels*, 2018, **32**, 11362–11374.

32 X. Zhu, Y. Wei, H. Wang and K. Li, *Int. J. Hydrogen Energy*, 2013, **38**, 4492–4501.

33 T. Shen, H. Ge and L. Shen, *Int. J. Greenhouse Gas Control*, 2018, **75**, 63–73.

34 J. Riley, R. Siriwardane, H. Tian, W. Benincosa and J. Poston, *Appl. Energy*, 2018, **228**, 1515–1530.
35 D. Zeng, Y. Qiu, S. Peng, C. Chen, J. Zeng, S. Zhang and R. Xiao, *J. Mater. Chem. A*, 2018, **6**, 11306–11316.
36 R. Pérez-Vega, A. Abad, M. T. Izquierdo, P. Gayán, L. F. de Diego and J. Adánez, *Appl. Energy*, 2019, **237**, 822–835.
37 D. Zeng, Y. Qiu, M. Li, L. Ma, D. Cui, S. Zhang and R. Xiao, *Appl. Catal., B*, 2021, **281**, 119472.
38 W. C. Cho, J. K. Lee, G. D. Nam, C. H. Kim, H. S. Cho and J. H. Joo, *Appl. Energy*, 2019, **239**, 644–657.
39 D. Zeng, Y. Qiu, L. Ma, M. Li, D. Cui, S. Zhang and R. Xiao, *Environ. Sci. Technol.*, 2020, **54**, 12467–12475.
40 R. Bharati, R. A. Singh and B. M. Wanklyn, *J. Mater. Sci.*, 1981, **16**, 775–779.
41 A. K. Bhattacharya, R. G. Biswas and A. Hartridge, *J. Mater. Sci.*, 1997, **32**, 353–356.
42 R. Bharati, R. A. Singh and B. M. Wanklyn, *J. Phys. Chem. Solids*, 1982, **43**, 641–644.
43 T. De Los Ríos Castillo, J. Salinas Gutiérrez, A. López Ortiz and V. Collins-Martínez, *Int. J. Hydrogen Energy*, 2013, **38**, 12519–12526.
44 A. López-Ortiz, P. E. González-Vargas, M. J. Meléndez-Zaragoza and V. Collins-Martínez, *Int. J. Hydrogen Energy*, 2017, **42**, 30223–30236.
45 T. De Los Ríos-Castillo, L. C. Palacios, S. A. De Los Ríos, D. D. Vigil, J. S. Gutiérrez, A. L. Ortiz and V. Collins-Martínez, *J. New Mater. Electrochem. Syst.*, 2009, **12**, 55–61.
46 H. M. Ahmed, A.-H. A. El-Geassy, N. N. Viswanathan and S. Seetharaman, *ISIJ Int.*, 2011, **51**, 1383–1391.
47 A. Lopez-Ortiz, M. J. Meléndez-Zaragoza, J. M. S. Gutiérrez, P. E. González-Vargas and V. Collins-Martínez, *Int. J. Hydrogen Energy*, 2019, **44**(24), 12315–12323.
48 Z. Song, J. Ma, H. Sun, W. Wang, Y. Sun, L. Sun, Z. Liu and C. Gao, *Ceram. Int.*, 2009, **35**, 2675–2678.
49 H. M. Ahmed and S. Seetharaman, *Int. J. Mater. Res.*, 2011, **102**, 1336–1344.
50 H. M. Ahmed and S. Seetharaman, *Metall. Mater. Trans. B*, 2010, **41**, 173–181.
51 V. H. Collins-Martinez, J. F. Cazares-Marroquin, J. M. Salinas-Gutierrez, J. C. Pantoja-Espinoza, A. Lopez-Ortiz and M. J. Melendez-Zaragoza, *RSC Adv.*, 2021, **11**, 684–699.
52 H. Putz and K. Brandenburg, *Cryst. Impact Softw*.
53 H. Kang, Y.-K. Jeong and S.-T. Oh, *Int. J. Refract. Met. Hard Mater.*, 2019, **80**, 69–72.
54 J. M. Quintana-melgoza, J. Cruz-reyes and M. Avalos-borja, *Mater. Lett.*, 2001, **47**, 314–318.
55 T. Ishihara, H. Kusaba, H. H. Kim and B. S. Kang, *ISIJ Int.*, 2019, **59**, 613–618.
56 H. M. Ahmed, A.-H. A. El-Geassy and S. Seetharaman, *Metall. Mater. Trans. B*, 2010, **41**, 161–172.
57 S. Inomata and M. Kajihara, *J. Alloys Compd.*, 2011, **509**, 4958–4966.
58 O. Levenspiel, *Ind. Eng. Chem. Res.*, 1999, **38**, 4140–4143.
59 S. Sridhar, D. Sichen and S. Seetharaman, *Metall. Mater. Trans. B*, 1994, **25**, 391–396.
60 J. Wendel, Thermodynamics and kinetics of tungsten oxidation and tungsten oxide sublimation in the temperature interval 200–1100 °C, Master's thesis, 2014.
61 G. R. Smolik, *Tungsten alloy oxidation behavior in air and steam: Fusion Safety Program/activation products task*, EG and G Idaho, Inc., Idaho Falls, ID (United States), 1992.
62 G. R. Smolik, K. A. McCarthy, D. A. Petti and K. Coates, *J. Nucl. Mater.*, 1998, **258–263**, 1979–1984.
63 J. L. Sabourin and R. A. Yetter, *J. Propul. Power*, 2011, **27**, 1088–1096.
64 E. Lorente, J. A. Peña and J. Herguido, *J. Power Sources*, 2009, **192**, 224–229.
65 D. Zeng, M. Li, Y. Qiu, L. Ma, D. Cui, S. Zhang and R. Xiao, *Int. J. Hydrogen Energy*, 2020, **45**, 2034–2043.
66 Z. Huang, Z. Deng, D. Chen, G. Wei, F. He, K. Zhao, A. Zheng, Z. Zhao and H. Li, *ACS Sustainable Chem. Eng.*, 2019, **7**, 11621–11632.